A Comprehensive Numerical and Experimental Study for the Passive Thermal Management in Battery Modules and Packs

Jinyong Kim,[1,z] Chuanbo Yang,[1,*] Joshua Lamb,[2] Andrew Kurzawski,[2] John Hewson,[2,*] Loraine Torres-Castro,[2] Anudeep Mallarapu,[1] and Shriram Santhanagopalan[1,*]

[1]*Center for Energy Conversion and Storage Systems, National Renewable Energy Laboratory, Golden, Colorado 80401, United States of America*
[2]*Sandia National Laboratories, Albuquerque, New Mexico 87185, United States of America*

Cooling plates in battery packs of electric vehicles play critical roles in passive thermal management systems to reduce risks of catastrophic thermal runaway. In this work, a series of numerical simulations and experiments are carried out to unveil the role of cooling plates (both between cells and a bottom plate parallel to the cell stack) on the thermal behavior of battery modules and packs under nail penetrations. First, we investigated the role of side cooling plates on the thermal runaway propagation mitigation in battery modules (1S3P) and packs (3S3P) by varying the key parameters of the side cooling plates, such as plate thicknesses, thermal contact resistances, and materials. Then, three important factors for passive thermal management systems are identified: (i) thermal mass of side cooling plates, (ii) interfacial thermal contact resistances, and (iii) the effective heat transfer coefficients at exterior surfaces. The roles of bottom cooling plates on thermal runaway propagation mitigation in 1S3P and 1S5P battery modules are numerically investigated by comparing the thermal behavior of the modules with only side cooling plates and with both side and bottom cooling plates.

Safety of the battery packs in electric vehicles is one of the most critical concerns for the commercialization of electric vehicles (EV).[1–3] For example, sudden Joule heating due to local mechanical or thermal failure due to an EV crash can cause a dramatic increase in local cell temperature,[4–10] which in turn triggers exothermal thermal abuse reactions and volatile gas generations when the local temperature exceeds $160 \sim 200 °C$. If a thermal management system of a battery pack fails to alleviate hot spots, those hot spots can cause cascading thermal runaway propagation through the entire battery pack. Moreover, turbulent oxidation of volatile gas generated during thermal runaway event can cause catastrophic fires in commercial EVs,[11–15] posing serious safety concerns.[16–18] Therefore, the design of safe thermal management systems for battery packs is of great importance for successful widespread adoption of EVs.

For safe battery-system design, it is important to understand the physical behavior of battery cells, modules, and packs during thermal runaway. Several recent modeling[10,15,19–23] and experimental efforts[24–29] have studied the physical behavior during thermal runaway, such as gas venting,[13,15,23] gas-phase reactions,[15] and exothermic thermal abuse reactions.[19,20] Various thermal runaway initiation methods have been considered in those studies including as nail penetrations,[9,10,22,28,30] internal short-circuit devices,[12,21] thermal ramp,[14] and over-charge.[14,31] Using the experimentally obtained data, such as temperature history during thermal ramps and accelerating rate calorimetry (ARC), parameters for thermal abuse models can be calibrated.[32] Then, the calibrated models can be utilized to study thermal runaway propagations in battery cells, modules, and packs.[33,34]

In particular, Li et al.[33] developed a three-dimensional (3D) electrochemical-thermal model to unveil the role of passive thermal management system in thermal behavior of a 1S5P module after a nail penetration. In this passive thermal management system, metallic inserts are placed as side cooling plates between cells, which are designed to absorb excessive heat and delay the heat transfer between cells to mitigate thermal runaway propagation. Moreover, Li et al.[33]

and Kurzawski et al.[34] found out that the thermal mass of the side cooling plates and the delay of heat transfer through thermal contact resistance at the surface between side cooling plates and cells ("gap effect") are the key factors of the passive thermal management system. Li et al.[33] numerically demonstrated that inserting thick aluminum plates (3.2 mm) for side cooling plates can mitigate the thermal runaway propagation from a cell under nail propagation to the adjacent cell. More recently, Yang et al.[35] conducted both modeling and experimental study of the role of side plates made from polyurethane foams on the delay of thermal runaway propagations. In this passive thermal management system, the optimization of the geometrical parameters of side cooling plates is the key since it directly influences the pack energy density, and hence the weight and the driving range of an EV. Therefore, a further investigation of the role of side cooling plates by conducting a parametric study is essential. Also, the role of bottom cooling plates, which act as heat sinks/distributor[36] of battery modules/packs and also flow-fields for coolant flow,[37] need to be also investigated considering that they are widely adopted in EV's thermal management system.

In this work, numerical and experimental studies are carried out to elucidate the roles of the both side and bottom cooling plates in the passive thermal management systems on the mitigation of cell-to-cell and module-to-module thermal runaway propagation. The numerical battery safety model based on the multi-scale multi-domain (MSMD) approach[33] is implemented. We consider a nail penetration as a damage initiation mechanism in this study. The role of side cooling plates are studied first both experimentally and numerically. Temporal evolutions of temperatures and voltages during nail penetration are simulated using numerical model, which is compared and validated against experimental results. Then, a safety map is presented to study the interplay among the three key factors of the passive thermal management system with side cooling plates; (i) thermal mass of side cooling plates, (ii) thermal contact resistances, and (iii) convective heat transfer coefficients. Then, using the numerical model validated by a secures of experimental results, we study the role of bottom cooling plates in passive thermal management systems by comparing the thermal behavior of battery modules with bottom cooling plates against the battery modules without bottom cooling plates.

*Electrochemical Society Member.
zE-mail: jxk621@alumni.psu.edu
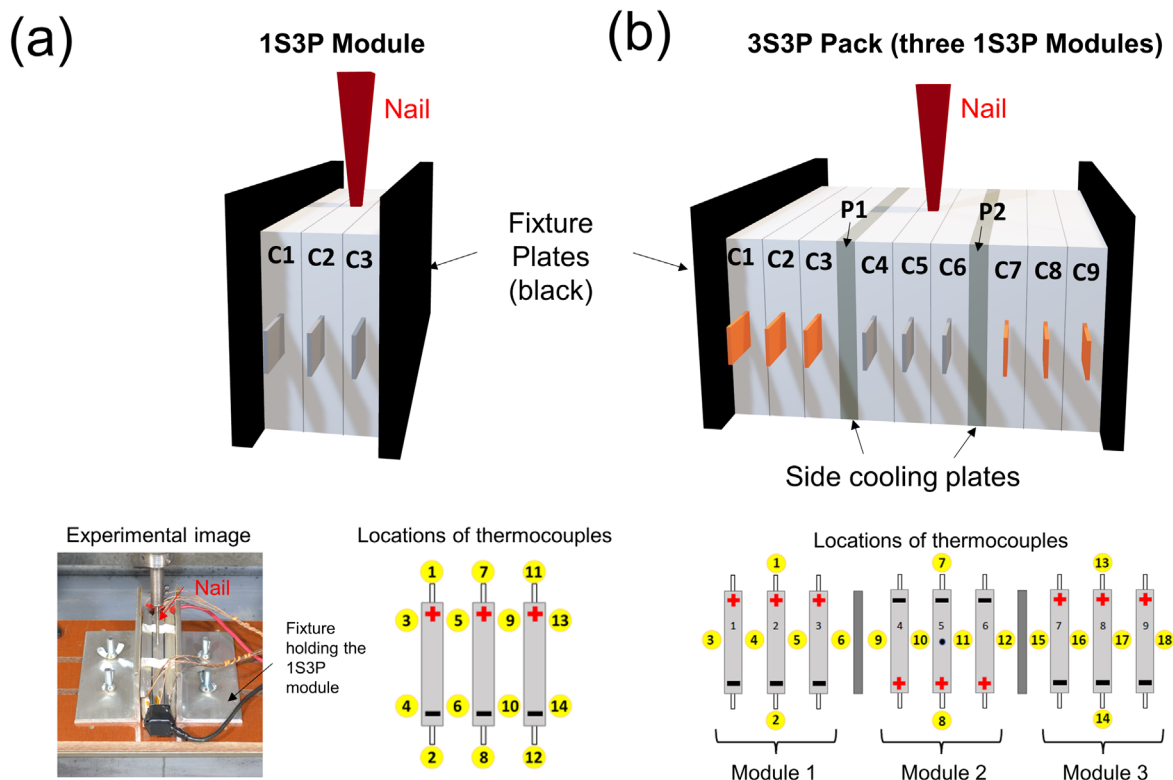
Figure 1. Schematic descriptions and locations of thermocouples for (a) 1S3P module and (b) 3S3P pack with three 1S3P modules.

Numerical Model

The current electrochemical-thermal model based on the multi-scale multi-domain (MSMD) framework solves two equations for potential in the positive (Φ_+) and negative electrodes ($\Phi-$) and one energy equation for temperature (T).[33,38]

$$0 = \nabla \bullet (\sigma_+ \nabla \phi_+) + j_{EC} - j_{short} \qquad [1]$$

$$0 = \nabla \bullet (\sigma_- \nabla \phi_-) - j_{EC} + j_{short} \qquad [2]$$

$$\frac{\partial(\rho c_p T)}{\partial t} = \nabla \bullet (k_{eff} \nabla T) + \dot{S}_{EC} + \dot{S}_{ab,i} + \dot{S}_{short} \qquad [3]$$

The detailed description of all physical properties, constitutional relationships, and source terms are listed in Refs. 20, 33, 38, and hence are not repeated here. Thermal properties and parameters related to heat transfer used in the current simulations are shown in Table I.

The current numerical model is validated against the data obtained from a wide set of experiments. All simulations and experiments are conducted with 5Ah Kokam Graphite/NMC cells (Model number: SLPB 11543140H5) at 100% SOC. The width, height, and thickness of the 5Ah Kokan cells are 142 ± 0.5 mm, 42.5 ± 0.5 mm, and 11.5 ± 0.2 mm, respectively, according to the manufacturer. However, considering the stacking, we use slightly reduced thickness of 10.5 mm for the cell. The nominal voltage and the weight of the cells are 3.7 V and 128 g, respectively. The volumetric and gravimetric energy densities of the cells are 266.6 Wh L^{-1} and 144.5 Wh kg^{-1}, respectively.

Figure 1 shows schematic descriptions of the 1S3P module and the 3S3P pack (with three 1S3P modules) used in both experiments and simulations Model parameters, such as thermal contact resistance between components and convective heat transfer coefficients, are calibrated based on the experimental results for the 1S3P module cases. These same model parameters are applied for the other cases if not indicated otherwise. In the experiments, metallic inserts are

placed between 1S3P modules in 3S3P packs and the two different materials for the metallic inserts, aluminum and copper, are considered.

The Newman, Tiedemann, Gu, and Kim (NTGK)[39,40] model is selected for the electrochemical model. NTGK model parameters are fitted against a wide range of discharge curves reported by the manufacturer, which is listed in Table II. Figure S1 compares the discharge curves from the manufacturer and the current NTGK model.

In particular, a four-equation thermal abuse reaction model developed by Hatchard et al.,[19] which was later implemented by Kim et al.[20] in three-dimensions, is considered. The rate of thermal abuse reactions (Eq. 4) and the corresponding exothermal heat sources (Eq. 5) of the four reactions are expressed as:

$$\frac{d\overline{c_i}}{dt} = -A_i(\overline{c_i})^{m_i} \exp\left(\frac{-E_{a,i}}{RT}\right) = -\dot{S}_i \qquad [4]$$

$$\dot{S}_{ab.i} = H_i W_i \dot{S}_i \qquad [5]$$

where $\overline{c_i}$ is a normalized concentration of ith reactive material. Detailed descriptions of thermal abuse reaction parameters are found in Refs. 19 and 20. The parameters used in the present simulations are listed in Table III.

In particular, we adopted a Patanker-Runge–Kutta scheme derived by Burchard et al.[41] to solve Eq. 4, which is a second-order scheme that ensures normalized concentrations ($\overline{c_i}$) are unconditionally positive during integrations. Specifically, we use smaller time-steps for integration of thermal abuse reaction equations (Eq. 4), 1/10 of the electrochemical-thermal time-step (Eqs. 1–3), to ensure the high accuracy of the numerical solutions. To test the accuracy of the present numerical scheme, we consider a simulation case with a cell at the initial temperature of 177 °C (450 K). The cell is at adiabatic condition and is subject to thermal runaway due to high temperature. Then, the temporal evolutions of average cell temperatures with different electrochemical-thermal timesteps using the present

Table I. Thermal properties of materials and modeling parameters for heat transfer.

Thermal properties of materials

Descriptions	Density, ρ [kg-m^{-3}]	Heat capacity, c_p [J-kg^{-1}°C^{-1}]	Thermal conductivity, k [W-m^{-1}°C^{-1}]	Remarks
Jellyroll	2235	908	0.8(cross-plane) 27(in-plane)	
Copper	8978	381	387.6	Used in negative tab and side cooling plates
Aluminum	2719	871	202.4	Used in positive tab and side cooling plates

Modeling parameters related to heat transfer (baseline case)		
Descriptions	Values	Remarks
Convective heat transfer coefficient [W m^{-2}-°C^{-1}]	20	Applied at all exteriors
Emissivity [−]	0.8	Applied at all exteriors
Area-specific thermal contact resistances [m^2°C-kW^{-1}]	2.70 (jellyroll & jellyroll)	Applied at the interfaces between components
	2.70 (jellyroll & cooling plates)	
	10.8 (jellyroll & fixture plates)	

Table II. Description and parameters for NTGK model (I is discharging current of a cell [A]).

	NTGK model description	
	$I = Y(DoD)((U(DoD) - V_{cell}))$	
Parameters	Equilibrium potential (U [V])	Cell conductance (Y [S])
Mathematical form	$U = \sum_{n=0}^{9} a_n(DoD)^n$	$Y = \sum_{n=0}^{9} b_n(DoD)^n$
Degree 0	4.15769062	296.7345
Degree 1	−0.29926436	−789.956
Degree 2	−25.31560787	−6728.37
Degree 3	276.87443841	92832.57
Degree 4	−1449.82631802	−338877
Degree 5	4178.72183707	556993.7
Degree 6	−6897.45600959	−430965
Degree 7	6454.73600453	127257.5
Degree 8	−3164.30337476	0
Degree 9	625.48941701	0

numerical scheme are plotted in Fig. S2. By adopting the Patanker-Runge–Kutta scheme, high accuracy is achieved even with an electrochemical-thermal timestep as large as 0.5 s. Based on this observation, we select the time step of 0.2 s and 0.5 s for the validation of the present numerical model and the following parametric study in later sections, respectively.

In the present simulations, we assume that the fixture plates for the battery modules have infinite thermal mass since the fixture plates and the desk holding the battery modules have (i) much larger thermal mass than the battery modules as shown in Fig. 1a and (ii) have very high thermal conductivity ($\sim$50 W-m^{-1}°C^{-1} for steel). Hence, constant temperature for the fixture plates is assumed and the fixtures are not explicitly modeled in the numerical simulations. We set the temperature of the fixtures and the ambient temperature to 25 °C (298 K) throughout the simulations.

The transport equations (Eqs. 1–3) are numerically discretized and solved by a commercial CFD software, Ansys Fluent® version 19.2.[42] Electrochemical/thermal modeling parameters and source terms are implemented using user-defined-functions (UDF). In all simulations, residuals for positive, negative potentials, and energy equations below 1E-8, 1E-8, and 1E-6 are achieved, respectively, which serve as convergence criteria. We assume that the nail penetration process is fast and completes before the onset of thermal events, and hence temporal mechanical deformations during nail penetration are not considered. The short-circuit current and the corresponding Joule heating at the location of the nail penetration are modeled by prescribing a volumetric short-circuit resistances (R_{sc}) of 2.5E-8 Ohm-m^3. Then, the corresponding electrochemical (Eq. 6) and thermal source terms (Eq. 7) in the governing equations (Eqs. 1–3) due to the nail penetration are expressed as:

$$j_{short} = \frac{\phi_+ - \phi_-}{R_{sc}} \quad [6]$$

$$\dot{S}_{short} = \frac{(\phi_+ - \phi_-)^2}{R_{sc}} \quad [7]$$

Experimental Setup

Propagation testing was based on tests of 5 Ah pouch format cells with an NMC-based cathode and a graphite anode, built into 1S3P individual modules. The three 1S3P modules are configured in a 3S3P pack for performing module-to-module propagation tests. Cells and modules are fixed hand-tight without a specific stack pressure. Figure 1 shows the general layout of the test modules along with numbered thermocouple locations. K-type thermocouples were used to measure the temperatures of the regions of interest. Initiation was performed on the central cell of the battery (Cell 2 in Fig. 1a and Cell 5 in Fig. 1b). Monitoring during propagating failure included module and pack voltage, temperature monitoring at the numbered thermocouples, and visual recording of the failure as it progressed through the pack. Baseline testing was performed on single 1S3P modules and propagation mitigation was evaluated by placing plates at the locations indicated. Details on the material and thicknesses for the side cooling plates are provided in subsequent sections. Nail penetration was used to establish an initial failure leading to thermal runaway at near-ambient conditions in all experimental tests.

Results and Discussion

Model validation.—Figure 2 first compares the experimental and simulated voltage and temperature behavior of the 1S3P module, which is designed to study cell-to-cell damage propagation. Figure 2a shows the comparison in voltage behavior. In simulations, the voltage drops gradually right after the nail penetration starts, while the experiment shows fluctuating voltages after the nail penetration, which eventually drop to zero.

The temperature trends between the numerical model and experiments agree well as shown in Fig. 2b. The arrangement of thermocouple locations is shown in Fig. 1a. It takes about 20 s for thermal runaway to propagate from the interface between the trigger cell (cell 2) and an adjacent cell (cell 3, TC 9) to the interface between the cell 3 and the fixture (TC 13) along the thickness directions, based on the difference in times between when the temperatures of thermocouples reach their maximum, which means that a characteristic time scale for cell-to-cell damage propagation is about 20 s for the combined cell-crossing and gap-crossing in the current case.

Comparisons are also made for the 3S3P packs, in order to validate the numerical model in a more comprehensive manner and to study the thermal behavior during module-to-module damage propagation. Two different materials for side cooling plates are considered; 3.2 mm Al plates and 3.2 mm Cu plates, where the Cu plates have approximately 40% more thermal mass than Al plates. As shown in Fig. 3a (Al plates) and Fig. 3c (Cu plates), the numerical model captures the experimental trends well in terms of thermal runaway propagation intervals and maximum temperature rise.

The comparison of voltage trends shows that the current numerical model can predict the temporal behavior of cascading thermal runaway between modules, since the current model captures the time when module 1 starts to fail. In the case of Al plates between modules (Fig. 3b)**,** it takes $\sim$75 s for Module 1 to fail after Module 2 fails, while it takes $\sim$ 95 s in the case of Cu plates between

Table III. Thermal abuse reaction parameters.

Description	Symbol	Value	Units	References
SEI decomposition reaction				
Pre-exponential factor	A_{SEI}	1.667E15	s^{-1}	20
Activation energy	E_{SEI}	1.3508E5	$J\ mol^{-1}$	20
Reaction order	m_{SEI}	1.00	—	20
Heat of reaction	H_{SEI}	257	$J\ g^{-1}$	20
Specific carbon content	W_C	7.32E5	$g\ m^{-3}$	adjusted
Initial value for normalized concentration	$\overline{C_{SEI}}$	0.15	—	20
Negative-solvent reaction				
Pre-exponential factor	A_{ne}	2.5E13	s^{-1}	20
Activation energy	E_{ne}	1.3508E5	$J\ mol^{-1}$	20
Reaction order	m_{ne}	1.000	—	20
Heat of reaction	H_{ne}	1714	$J\ g^{-1}$	20
Specific carbon content	W_C	7.32E5	$g\ m^{-3}$	adjusted
Initial value for normalized concentration	$\overline{C_{ne}}$	0.75	—	20
Initial value of t_{sei}	$t_{sei,0}$	0.033	—	20
Reference value of t_{sei}	$t_{sei,ref}$	0.033	—	20
Positive-solvent reaction				
Pre-exponential factor	A_{pe}	6.667E13	s^{-1}	20
Activation energy	E_{pe}	1.396E5	$J\ mol^{-1}$	20
Reaction order for $\bar{\alpha}$	$m_{1,pe}$	1.000	—	20
Reaction order for $1 - \bar{\alpha}$	$m_{2,pe}$	1.000	—	20
Heat of reaction	H_{pe}	314	$J\ g^{-1}$	20
Specific content for positive active material	W_P	1.465E7	$g\ m^{-3}$	adjusted
Initial value of $\bar{\alpha}$	$\overline{\alpha_0}$	0.04	—	20
Electrolyte decomposition reaction				
Pre-exponential factor	A_{el}	5.14E25	s^{-1}	20
Activation energy	E_{el}	2.74E5	$J\ mol^{-1}$	20
Heat of reaction	H_{el}	155	$J\ g^{-1}$	20
Specific content for electrolyte	W_{el}	4.88E5	$g\ m^{-3}$	adjusted
Initial value for $\overline{C_e}$	$\overline{C_{e,0}}$	1	—	20
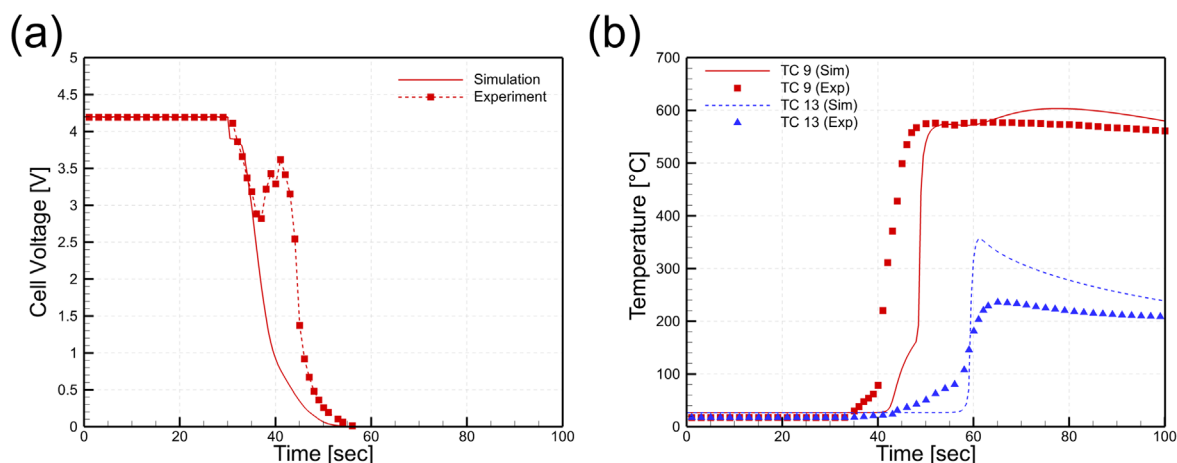
Figure 2. Comparison of (a) cell voltage and (b) thermocouple temperatures between experimentally measured data and simulations in the case of a 1S3P module.

modules (Fig. 3d). This is primarily due to the 40% larger thermal mass of Cu plates, compared to Al plates.

The role of side cooling plates.—As noted in the experimental and numerical studies in the previous section, passive thermal runaway management can be helpful for improving battery safety. Here, we identify three parameters that play critical roles in passive thermal runaway management with side cooling plates:

• Thermal mass of side cooling plates:

    o. Metallic inserts such as side cooling plates absorb excessive heat generated during thermal abuse reactions.

• Thermal contact resistance:

    o. Increasing thermal contact resistance at interfaces between the components (cell-to-side cooling plates or cell-to-cell) reduces the rate of heat transfer from the damaged cell to the adjacent
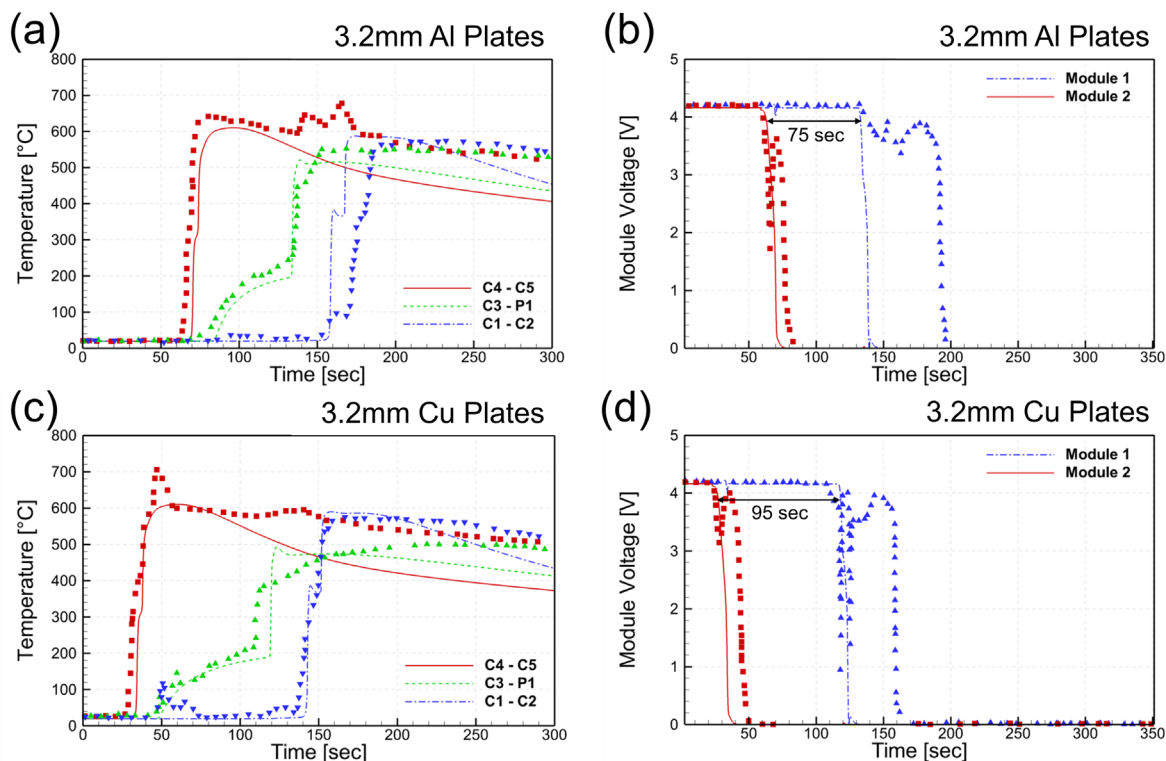
Figure 3. Comparisons of (a), (c) voltages and (b), (d) thermocouple temperatures between experimentally measured data (*symbols*) and the simulated data (*lines*) in the case of the 3S3P pack (Figs. 3a–3b: 3.2 mm aluminum plates, Figs. 3c–3d: 3.2 mm cooper plate).

cell, causing a "gap effect." A larger "gap effect" results in more time for heat removal.

• Heat removal rate:

   o. Natural convection and radiation at the external surfaces remove heat generated during thermal abuse reactions. Higher rates of such heat removal are favorable for battery safety. Heat can also be dissipated to structural materials and cooling systems as discussed below.

In order to numerically study the effect of those three parameters in detail, 1S3P modules with metallic inserts as side cooling plates between cells are considered and shown schematically in Fig. 4a. A wide range of parameter values for the (i) thicknesses for side cooling plates, (ii) material choices for side cooling plates, (iii) thermal contact resistances between cells and side cooling plates and (iv) effective heat transfer coefficients are considered in the simulations, while the other conditions such as cell dimensions and electrochemical parameters remain same.

Figure 4b first compares the temporal evolution of the average cell temperatures with different thermal contact resistances to study the "gap" effect on the thermal runaway propagation mitigation. In the case of the lowest thermal contact resistance (1.35 m^2°C kW^{-1}), thermal runaway propagation mitigation is not achieved and the cell crossing time is 50 s (Cell-to-cell propagation time is defined as the difference in times when the damaged cell and the adjacent cell reach their own maximum average temperatures. In comparison to Torres-Castro et al. [8] the cell-crossing time here would be the sum of the cell-crossing time and gap-crossing time in [8]). Increasing the thermal contact resistance slows the heating of the next cell while the initial cell is able to cool further. At $R_{th} > 5.40$ m^2°C kW^{-1}, thermal runaway propagation mitigation is observed. In summary, higher thermal contact resistances result in progressively increasing cell-to-cell propagation times, and hence larger fraction of the generated heat can be removed via heat dissipation.

The temporal evolution of the average temperature across the modules with different materials for side cooling plates is demonstrated in Fig. 4c. Similar to the results in the previous section (Fig. 3), using a copper plate for side cooling plates results in a slower temperature rise for the plates, and a consequently slower temperature rise in the adjacent cells (cells 1 and 3), which is primarily due to the fact that Cu plates have 40% larger specific heat capacity compared to Al plates. Unlike the results in the previous sections (Fig. 3), thermal runaway propagation mitigation is achieved here since the generated abuse heat at cell 2 is absorbed by two adjacent plates unlike the setup in the previous section.

To study the interactions among the three parameters on thermal runaway propagation mitigation, the minimum thicknesses of side cooling plates required for thermal runaway propagation mitigation are plotted in Fig. 5a by varying those parameters. We performed simulations by gradually decreasing the thickness of metallic inserts from 15 mm to 1 mm in 1 mm increments until the thermal runaway of adjacent cells (cell 1 and cell 3) occurs. If the temperatures of adjacent cells remain less than 200 °C for 10 min after the nail penetration in cell 2, we consider that thermal runaway propagation to be mitigated. In order to more closely focus on the thermal runaway propagation from the center trigger cell and more strictly control the heat dissipation to surroundings, we turned off the heat dissipation to the fixture by creating a perfectly insulating boundary condition since the effect of the heat dissipation to the fixture can be significant. Then, the heat dissipation is controlled only by varying the effective heat transfer coefficient at the remaining exterior surfaces.

This map can serve as a safety map for the design of the passive thermal management system, which is very important for module/pack design as the thickness of the side plate directly affects the energy density of the module/pack. To increase the module/pack energy density, the thickness of the side cooling plates needs to be reduced. As seen in Fig. 5a, the minimum thicknesses of the side cooling plates required for thermal runaway mitigation are determined by the three key parameters identified earlier. This map first
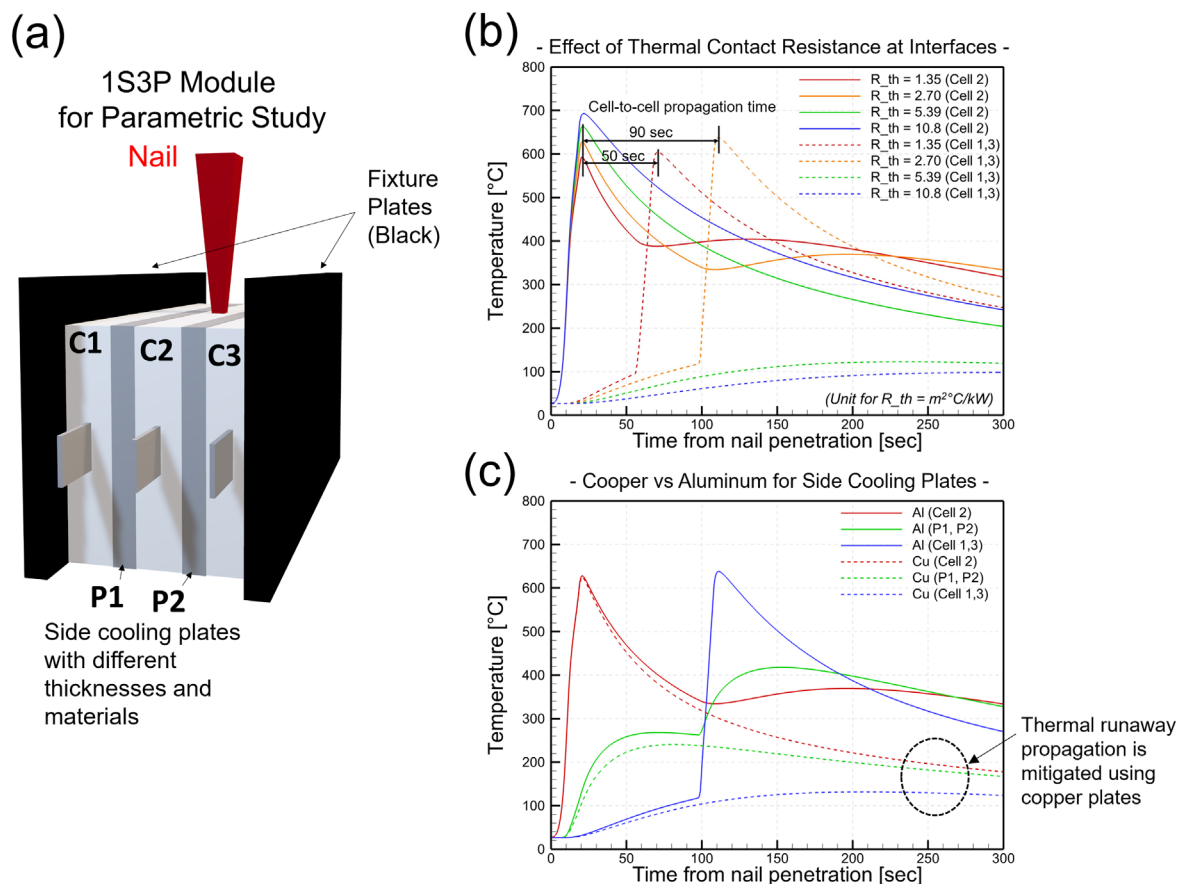
Figure 4. (a) Schematic of a 1S3P module with side cooling plates to study the role of three parameters associated with passive thermal management on thermal runaway mitigation. (b) Comparison of average cell temperature behavior at different area-specific thermal contact resistances (thickness of Al plates = 3.2 mm). (c) Comparison of average cell temperatures behavior between the case with Al plates and the case with Cu plates (R_{th} = 2.70 m^2°C-kW^{-1}, thickness of plates = 3.2 mm).

suggests the importance of heat dissipation on thermal runaway propagation mitigation. By increasing the effective heat transfer coefficients, the minimum thicknesses required for the side cooling plates can be reduced. At $h = 0$ W-m^{-2}°C^{-1} and $R_{th} = 0$ m^2°C-kW^{-1}, and with side plates being perfectly insulating, the minimum thickness required for the side cooling plates is very thick (15 mm), and hence a significant reduction in energy density is unavoidable. However, at $h = 40$ W-m^{-2}°C^{-1} and $R_{th} = 0$ m^2°C-kW^{-1}, this minimum thickness is significantly reduced to 5 mm, which implies module/pack energy density can be improved with better heat dissipation.

Increasing thermal contact resistance also helps to reduce the thicknesses of side cooling plates. As discussed previously, increasing thermal contact resistances results in a longer time for thermal runaway propagation, which leads to more heat dissipation before thermal runaway propagation. However, at low effective convective coefficient cases ($h = 0$ W-m^{-2}°C^{-1}), increasing thermal contact resistance does not help thermal runaway propagation mitigation. This means that only increasing the "gap effect" is not enough for the successful mitigation of thermal runaway propagation, although this allows passengers and drivers more time to escape from the damaged vehicles.

The effective volumetric and gravimetric module energy density reflecting the thicknesses of side cooling plates are shown in Figs. 5b and 5c, respectively. Poor convective heat removal and low interfacial thermal contact resistance result in a significant reduction in effective module energy density, which may cause detrimental effects on the driving range and acceleration of electric vehicles. For example, at $h = 0$ W-m^{-2}°C^{-1} and $R_{th} = 0$ m^2°C-kW^{-1}, the effective volumetric and gravimetric module packaging efficiencies (ratio between module

energy density to pure cell energy density) are only 51% and 46.3%, respectively. This means that inactive components account for 49% and 53.7% of the module's volume and weight However, high interfacial thermal contact resistance and high convective transfer coefficient significantly increase the effective module packaging efficiency. At $h = 40$ W-m^{-2}°C^{-1} and $R_{th} = 10.8$ m^2°C-kW^{-1}, effective volumetric and gravimetric module packaging efficiencies are 84% and 81.2%, respectively. It is interesting to note that these efficiencies are similar to the cell-to-pack ratios of battery packs using lithium iron phosphate (LFP) cathodes reported by Yang et al.[43] However, other inactive components, such as pack casing and cooling systems, should be accounted for a fair comparison.

The role of bottom cooling plates.—In the last section, we numerically studied the role of the three parameters of passive thermal management with side cooling plates on thermal runaway propagation mitigation. In this section, we investigate the role of a bottom plate, the plate that connects all the side cooling plates and battery cells in a module, on the mitigation of thermal runaway propagation. Figure 6 shows configurations of cooling plates of battery modules considered in this numerical model. Each of the four configurations has the same thermal mass for the combined cooling plates (side + bottom). We consider cases with "only side plates" and cases with "both side plates and bottom cooling plates." Also, two different module configurations, 1S3P and 1S5P, are considered since the performance of a bottom cooling plate can differ depending on the number of cells in a module. The energy densities of 1S3P modules and 1S5P modules are 163 Wh L^{-1} (81.52 Wh kg^{-1}) and 193 Wh L^{-1} (98.73 Wh kg^{-1}), respectively. We assume no thermal contact resistance between the side cooling plates and bottom
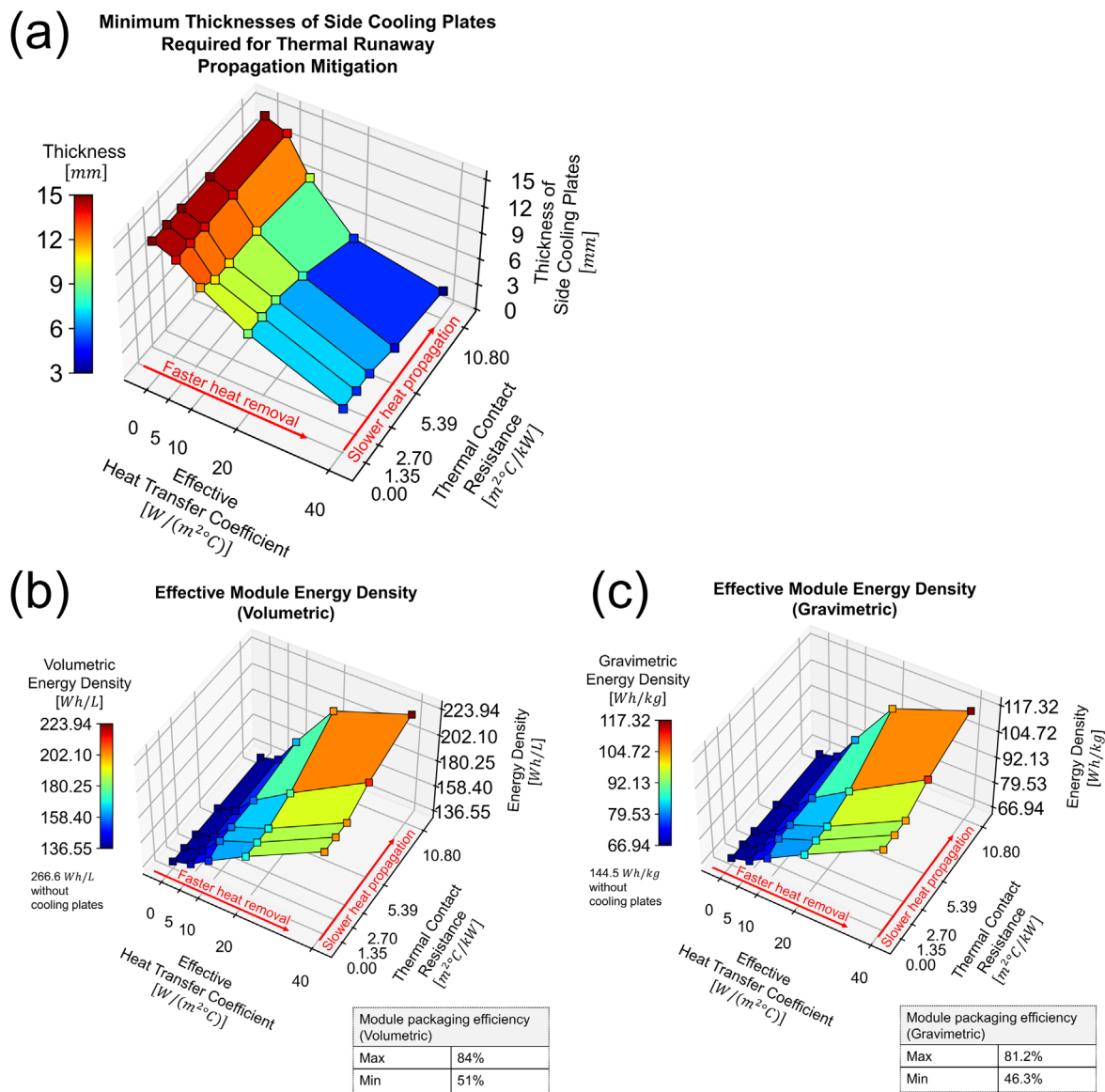
Figure 5. (a) Minimum thicknesses of side cooling plates required for thermal runaway propagation mitigation depending on area-specific thermal contact resistances and effective heat transfer coefficients. The corresponding (b) volumetric and (c) gravimetric effective module energy density. Aluminum metallic inserts are used for this example.

cooling plates. Then, thermal behaviors of the four different cases under nail penetrations are studied.

Figure 7 compares the temporal average cell temperature profiles of the four different cases. In cases with 1S3P modules for this configuration, the bottom plates are not helpful for preventing thermal runaway propagation as seen in Fig. 7a. With the same plate mass in both 1S3P scenarios, the scenario with the bottom plate absorbs similar energy but has a greater interfacial heat transfer area between the cell and the (side + bottom) plates. This results in faster heat transfer to the adjacent cell with the bottom plate leading to the quicker thermal runaway propagation noted in Fig. 7a.

However, shifting some of the plate mass to the bottom plates can be helpful for the 1S5P module in terms of thermal runaway propagation mitigation. As seen in Fig. 7b, cascading propagation of thermal runaway is observed in the case with only side cooling plates, while thermal runaway is successfully mitigated for the case with both side and bottom cooling plates. With the 1S5P module having plates only in between the cells, the actual mass of plate available to prevent propagation is less (the same mass is distributed over four rather than two plates) leading to faster propagation for

this case seen in Fig. 7b compared to the 1S3P seen in Fig. 7a. This shows that the mass in contact with a cell does play an important role in the time for propagation.

When the overall mass of the plates for the 1S5P module is split between plates between and bottom cooling plates, Fig. 7b shows that propagation is mitigated. This is an important result because in this scenario the total mass of the plates is divided into more cells; that is, the module volumetric energy density of the 1S5P module is ~18% greater than the 1S3P module (11.3% larger effective module packaging efficiency). The primary reason for such improvement in the propagation resistance is that the combined (side + bottom) plates are exposed to more (five vs three) cells. Heat is transferred rapidly through the metal plates and then more gradually to the cells because of their lower thermal conductivity. When the combined plates are exposed to five cells, less heat is transferred to the adjacent cells because some is transferred to cells beyond the adjacent cell. Because the cell mass is the dominant mass in the system, modest heating of additional cells has an important influence on the propagation resistance.
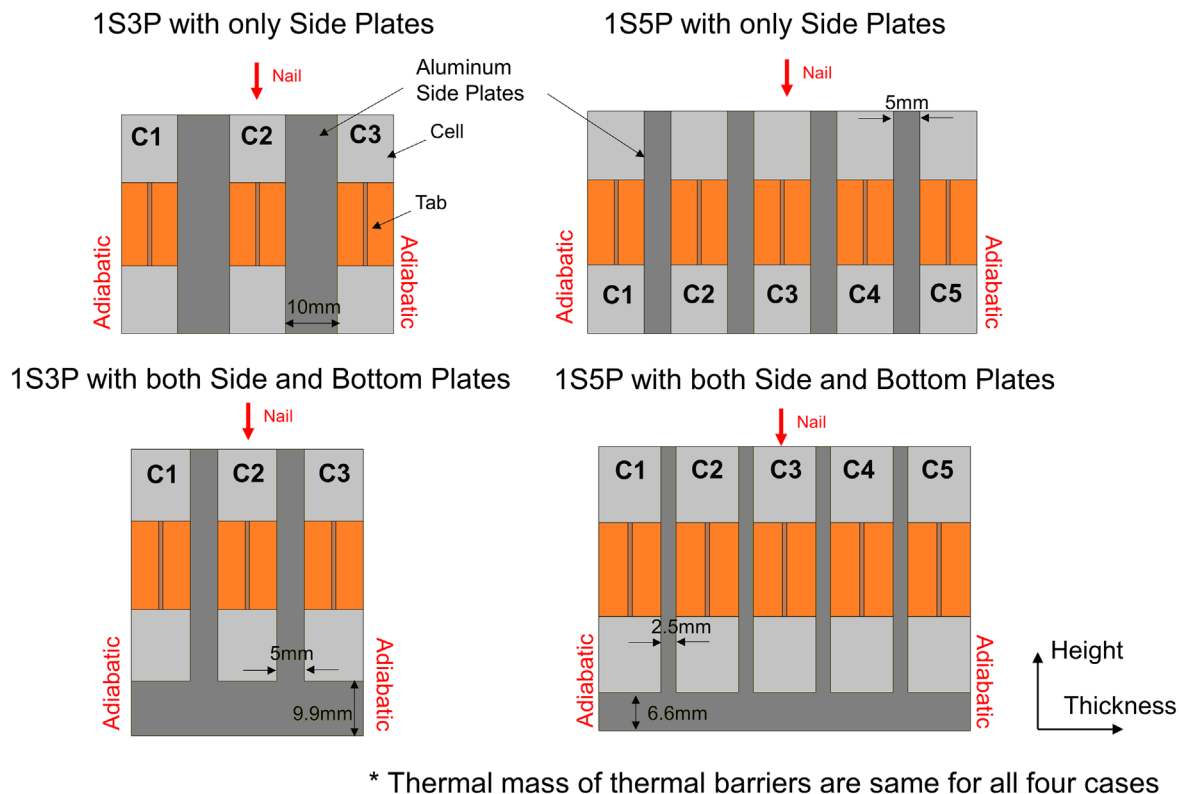
Figure 6. Schematics of the four configurations of battery modules considered to study the effect of bottom cooling plates on thermal runaway mitigation.
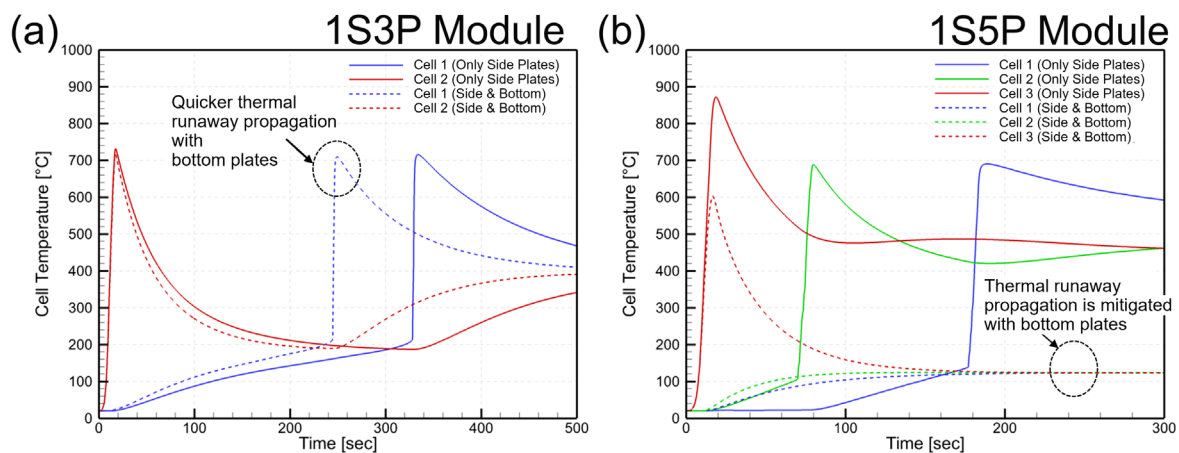

Figure 7. Comparison of average cell temperatures for the four different configurations of battery modules: (a) 1S3P with disconnected and connected metallic inserts (b) 1S5P with disconnected and connected metallic inserts.

To illustrate this in more detail, comparisons of the temporal evolution of temperature with the heat vectors at the cooling plates are made. Figure 8a (1S5P with only side cooling plates) shows that the excessive heat generated is only absorbed to the two adjacent side plates attached, and the direction of heat transport is mainly limited to the through-thickness direction of the cell. At 90 s (Fig. 8b), thermal runaway propagation is observed at the adjacent cells as they are sufficiently heated up to reach their onset temperature of thermal runaway.

However, the excessive heat generated during thermal runaway is transferred to the whole network of cooling plates as shown in Fig. 8c (1S5P with both side and bottom cooling plates), and heat transfer takes place both in the through-plane and in-plane directions. The heated plates are then able to distribute thermal energy to the additional cells, allowing the more uniform redistribution of

released heat. Also, owing to the relatively better heat removal from the damaged cell due to the larger interfacial area, the maximum temperature near the nail (750 °C) is much lower than the case with the only side plates (987 °C) at 30 s after the nail penetration. Due to the much larger total thermal mass of the combined five cells plus cooling plates attached to the damaged cell, thermal runaway propagation is successfully mitigated as seen in Fig. 8d.

Adopting concepts like these, allowing released heat to be spread over a broader range by using both side and bottom plates, can be helpful under the conditions that the battery pack is partially damaged, such as in a vehicle crash. The key roles of the plates, as discussed, is to (i) delay heat transport from damaged cells to their adjacent cell and to (ii) partially absorb the excessive heat generated due to thermal runaway. In recent studies, not only metal but also phase change materials and foam materials have been selected for
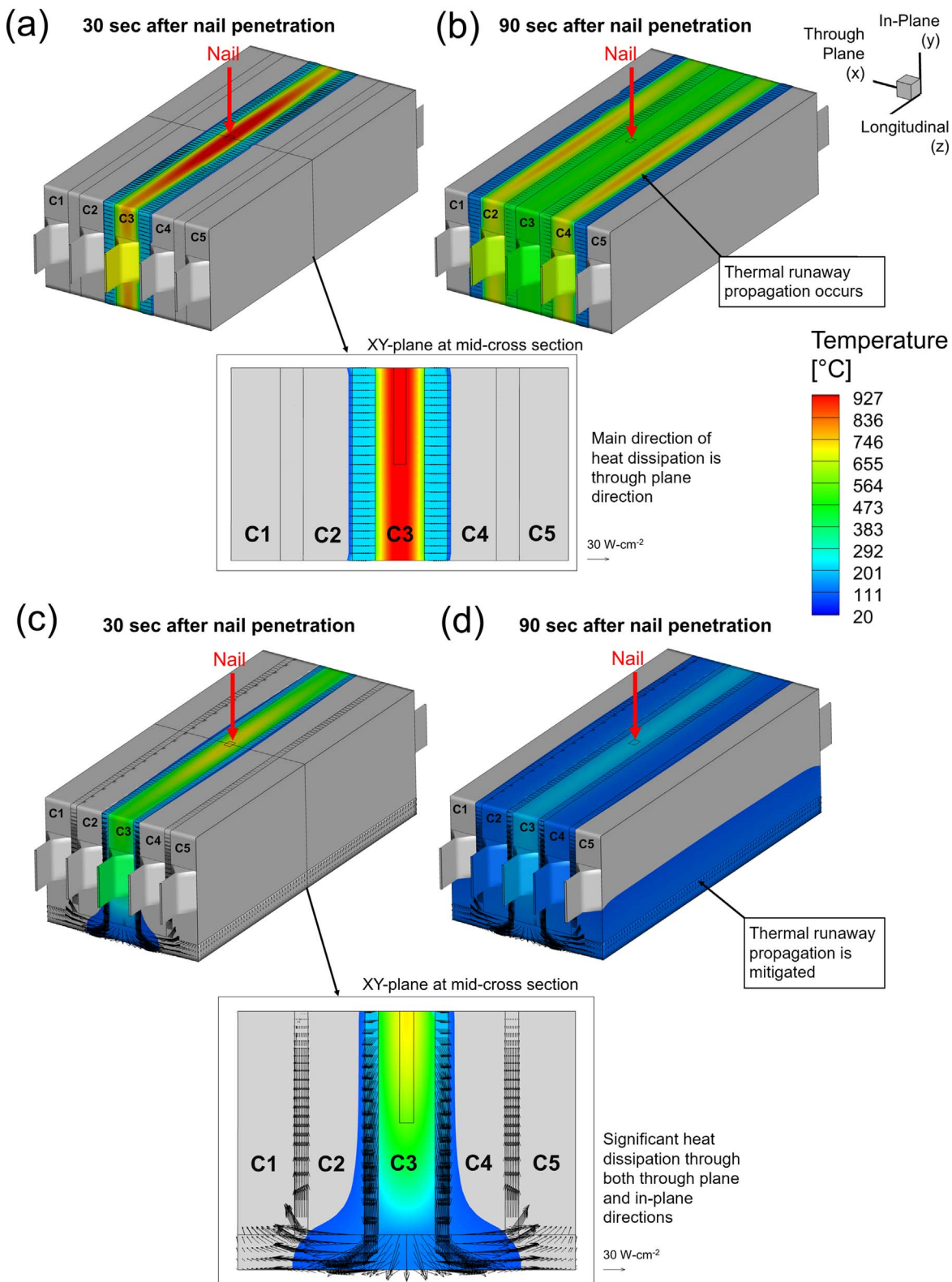
Figure 8. Temporal evolution of temperature and heat flux vector for 1S5P module with only side cooling plates (a) at 30 s after nail penetration and (b) at 90 s after nail penetration. Temporal evolution of temperature and heat flux vector for 1S5P module with both side and bottom cooling plates (c) at 30 s after nail penetration and (d) at 90 s after nail penetration. (cut-off temperature for the contour is 100 °C.)

side cooling plates.[44,45] Phase change materials act in a similar manner by absorbing thermal energy, with the potential benefit of absorbing more energy per mass. On the other hand, the role of the bottom cooling plates is to dissipate released heat over a broader range of both the plates and cells, but at a level that is less harmful. The results shown in Fig. 7 demonstrate that cooling plates are better optimized if the heat absorbed by them can be transmitted farther than the adjacent cells. Suppose the abuse heat is only allowed to be

transferred to the adjacent cells, as shown for the 1S3P module in Fig. 7 a. In that case, the bottom-plate effectiveness can actually be reduced because increased surface area allows for faster heat transfer.

In practical pack designs, the bottom cooling plates are often connected to gas/liquid cooling channels or car body parts. The former can increase the rate of heat dissipation, while the latter can help the absorption of excessive heat by further increasing the effective thermal mass. This numerical framework developed here is being extended to incorporate more large-scale thermal management systems to study the interplay among cell chemistry, thermal barrier design, and practical cooling system in upcoming future studies to solve the safety problem of the next generation EV's battery packs.

Conclusions

A series of numerical and experimental studies are conducted in order to understand the role of side and bottom cooling plates in the passive thermal management of battery packs in terms of thermal runaway propagation mitigations. The present study first focuses on the role of side cooling plates. The present numerical model is validated against a wide range of experiments conducted in Sandia National Laboratories. Then, a series of computations are made to study the role of three relevant parameters for passive thermal management with side cooling plates.

1. Thermal mass of side cooling plates: side cooling plates can absorb excessive heat generated at the damaged cell during thermal abuse reactions
2. Thermal contact resistances between the side cooling plates and the cells: a larger delay of thermal runaway propagation allows more time for heat removal, which favors propagation mitigation
3. Heat removal rate through effective convection heat transfer coefficients: without adequate heat dissipation, increasing thermal contact resistance does not stop the cascading thermal runaway

Then, we investigated the role of bottom cooling plates on the mitigation of thermal runaway propagation using the developed numerical model. We show that using bottom cooling plates can be helpful for the mitigation of thermal runaway propagation for the 1S5P module since the connection between the side and bottom cooling plates allows heat to be dissipated across a greater part of the system, including some heat to non-adjacent cells. It results in the increase of the total thermal mass attached to the damaged cell, hence the more effective distribution of abuse heat generated after nail penetration. Also, this connection to the bottom plate promotes heat transfer along the in-plane direction to the bottom plate where thermal energy can potentially be absorbed through cooling channels and the thermally massive car frame that can be attached to the bottom plate in practical design. However, using bottom plates is not helpful if the extent of the bottom plate is limited to the adjacent cells as shown for the 1S3P modules since the thermal mass of attached plates remains the same. This analysis suggests that optimization of thermal design using a combined numerical and experimental method can improve the safety of battery packs.

Acknowledgments

ORCID

Jinyong Kim https://orcid.org/0000-0002-9540-2197
Chuanbo Yang https://orcid.org/0000-0001-7961-9911
Joshua Lamb https://orcid.org/0000-0001-8426-0122
John Hewson https://orcid.org/0000-0003-4053-5774
Loraine Torres-Castro https://orcid.org/0000-0002-9267-8489

References

1. C. Arbizzani, G. Gabrielli, and M. Mastragostino, *J. Power Sources*, **196**, 4801 (2011).
2. T. M. Bandhauer, S. Garimella, and T. F. Fuller, *J. Electrochem. Soc.*, **158**, R1 (2011).
3. J. Zhang, L. Zhang, F. Sun, and Z. Wang, *IEEE Access*, **6**, 23848 (2018).
4. J. Lowy, *Phys.org* (2013), https://phys.org/news/2013-01-overcharging-batteries-eyed-boeing-mishaps.html.
5. D. H. Doughty, E. P. Roth, C. C. Crafts, G. Nagasubramanian, G. Henriksen, and K. Amine, *J. Power Sources*, **146**, 116 (2005).
6. D. H. Doughty, P. C. Butler, R. G. Jungst, and E. P. Roth, *J. Power Sources*, **110**, 357 (2002).
7. F. Ren, T. Cox, and H. Wang, *J. Power Sources*, **249**, 156 (2014).
8. J. A. Jeevarajan and S. Surampudi, *Lithium Batteries, Proceedings*, **99**, 694 (2000).
9. W. Zhao, G. Luo, and C.-Y. Wang, *J. Electrochem. Soc.*, **162**, A207 (2015).
10. J. Kim, A. Mallarapu, and S. Santhanagopalan, *J. Electrochem. Soc.*, **167**, 90554 (2020).
11. H. Chen, J. E. H. Buston, J. Gill, D. Howard, R. C. E. Williams, C. M. Rao Vendra, A. Shelke, and J. X. Wen, *J. Power Sources*, **472**, 228585 (2020).
12. D. P. Finegan et al., *J. Power Sources*, **417**, 29 (2019).
13. P. T. Coman, S. Mátéfi-Tempfli, C. T. Veje, and R. E. White, *J. Electrochem. Soc.*, **164**, A1858 (2017).
14. A. W. Golubkov, S. Scheikl, R. Planteu, G. Voitic, H. Wiltsche, C. Stangl, G. Fauler, A. Thaler, and V. Hacker, *RSC Adv.*, **5**, 57171 (2015).
15. J. Kim, A. Mallarapu, D. P. Finegan, and S. Santhanagopalan, *J. Power Sources*, **489**, 229496 (2021).
16. E. Musk, *Tesla Blog* (2013), https://www.tesla.com/blog/model-s-fire.
17. B. Liu, Y. Jia, C. Yuan, L. Wang, X. Gao, S. Yin, and J. Xu, *Energy Storage Mater.*, **24**, 85 (2019).
18. P. Sun, R. Bisschop, H. Niu, and X. Huang, *A Review of Battery Fires in Electric Vehicles* (Springer, Berlin: US) (2020).
19. T. D. Hatchard, D. D. MacNeil, A. Basu, and J. R. Dahn, *J. Electrochem. Soc.*, **148** (2001).
20. G. H. Kim, A. Pesaran, and R. Spotnitz, *J. Power Sources*, **170**, 476 (2007).
21. P. T. Coman, E. C. Darcy, C. T. Veje, and R. E. White, *J. Electrochem. Soc.*, **164**, A587 (2017).
22. A. Mallarapu, J. Kim, K. Carney, P. DuBois, and S. Santhanagopalan, *eTransportation*, **4**, 100065 (2020).
23. P. T. Coman, S. Rayman, and R. E. White, *J. Power Sources*, **307**, 56 (2016).
24. D. P. Finegan et al., *Adv. Sci.*, **5**, 1700369 (2018).
25. D. P. Finegan et al., *Nat. Commun.*, **6**, 6924 (2015).
26. D. P. Finegan, B. Tjaden, T. M. M. Heenan, R. Jervis, M. Di Michiel, A. Rack, G. Hinds, D. J. L. Brett, and P. R. Shearing, *J. Electrochem. Soc.*, **164**, A3285 (2017).
27. T. G. Zavalis, M. Behm, and G. Lindbergh, *J. Electrochem. Soc.*, **159**, 848 (2012).
28. R. Zhao, J. Liu, and J. Gu, *Appl. Energy*, **173**, 29 (2016).
29. E. Sahraei, R. Hill, and T. Wierzbicki, *J. Power Sources*, **201**, 307 (2012).
30. K. Chiu, C. Lin, S. Yeh, Y. Lin, and K. Chen, *J. Power Sources*, **251**, 254 (2014).
31. L. Huang, Z. Zhang, Z. Wang, L. Zhang, X. Zhu, and D. D. Dorrell, *J. Energy Storage*, **25**, 100811 (2019).
32. L. Torres-Castro, A. Kurzawski, J. Hewson, and J. Lamb, *J. Electrochem. Soc.*, **167**, 090515 (2020).
33. Q. Li, C. Yang, S. Santhanagopalan, K. Smith, J. Lamb, L. A. Steele, and L. Torres-Castro, *J. Power Sources*, **429**, 80 (2019).
34. A. Kurzawski, L. Torres-Castro, R. Shurtz, J. Lamb, and J. C. Hewson, *Proc. Combust. Inst.*, **38**, 4737 (2020).
35. C. Yang, N. Sunderlin, W. Wang, C. Churchill, and M. Keyser, *J. Power Sources*, **541**, 231666 (2022).
36. K. Li, C. Xu, H. Wang, C. Jin, X. Rui, S. Chen, X. Feng, L. Fan, and M. Ouyang, *Appl. Therm. Eng.*, **201** (2022).
37. Y. Chung and M. S. Kim, *Energy Convers. Manag.*, **196**, 105 (2019).
38. G. Kim, K. Smith, K. Lee, S. Santhanagopalan, and A. Pesaran, *J. Electrochem. Soc.*, **158**, A955 (2011).
39. W. H. Tiedemann and J. Newman, *Proc. - Electrochem. Soc.*, **79–1**, 39 (1979).
40. H. Gu, *J. Electrochem. Soc.*, **130**, 1459 (1983).
41. H. Burchard, E. Deleersnijder, and A. Meister, *Appl. Numer. Math.*, **47**, 1 (2003).
42. https://ansys.com/products/fluids/ansys-fluent.
43. X. G. Yang, T. Liu, and C. Y. Wang, *Nat. Energy*, **6**, 176 (2021).
44. J. Luo, D. Zou, Y. Wang, S. Wang, and L. Huang, *Chem. Eng. J.*, **430**, 132741 (2022).
45. J. Wang, Q. Huang, X. Li, G. Zhang, and C. Wang, *J. Energy Storage*, **40**, 102810 (2021).